


# Drifting Ionospheric Scintillation Simulation for L-Band Geosynchronous SAR

Feixiang Tang , Yifei Ji , *Member, IEEE*, Yongsheng Zhang, Zhen Dong , Zhaokai Wang, Qingjun Zhang ,  
Bingji Zhao , and Heli Gao

**Abstract**—An L-band geosynchronous synthetic aperture radar (GEO SAR) is susceptible to the ionospheric scintillation induced by ionospheric irregularities due to its lower carrier frequency. In particular, the drifting characteristic of the ionospheric irregularities makes this issue more complicated because the drifting velocity is comparable with the scanning velocity of ionospheric penetration points (IPPs) of GEO SAR. In this article, a drifting ionospheric scintillation simulator (DISS) is devised for producing L-band GEO SAR raw data affected by the drifting ionospheric scintillation phase and amplitude errors. The DISS is divided into a static scintillation transfer function (STF) generator, an IPP drifting offset indexer and a GEO SAR echo generator. Each azimuth echo of a point target is modulated by the complex STF versus the drifting IPP coordinate. Finally, two simulation experiments of the point-target and extended-target scenes are conducted to validate the effectiveness of the DISS. The results indicate that the drifting ionospheric irregularities present absolutely different artifacts and more serious decorrelations in L-band GEO SAR images, compared with the traditional L-band low-Earth-orbit (LEO) SAR.

**Index Terms**—Drifting ionospheric irregularities, geosynchronous synthetic aperture radar (GEO SAR), ionosphere, ionospheric scintillation.

## I. INTRODUCTION

THERE has been an increasing prospect in developing a geosynchronous synthetic aperture radar (GEO SAR) due to great advantages of great coverage and short revisit [1], [2], [3]. Most GEO SAR conceptual systems have planned to adopt the carrier frequency of L-band for higher interferometric coherence and higher sensitivity to deformations, soil moisture, and forest biomass, compared with operating at S-/C-/X-band [4], [5], [6], [7], [8], [9]. Nevertheless, adopting the L-band meanwhile brings about a negative factor of remarkable ionospheric

effects that will cause imaging and interferometric distortions for L-band spaceborne SAR [10], [11], [12], [13], [14]. Because the turbulence caused by the ionospheric effects can increase as the wavelength becomes longer.

The ionosphere is generally classified into the deterministic background structures on large scales and the statistic irregular structures on small and medium scales [12], [13], [14]. The background ionosphere mainly causes phase advance, group delay, dispersion, and Faraday rotation (FR). Various artifacts caused by background ionosphere have been captured in the products of Advanced Land Observing Satellite (ALOS) Phased Array type L-band Synthetic Aperture Radar (PALSAR) and ALOS-2 PALSAR-2, such as polarimetric distortions [14], [15], [16], azimuth offsets, interferometric decorrelation streaks, and phase errors [14]. In addition, due to the ultra-long synthetic aperture time and ultra-large illuminated areas, the impacts of spatially and temporally varying background ionosphere on GEO SAR imaging and interferometry become remarkable and have been deeply explored in existent research works [17], [18], [19], [20], [21].

The ionospheric irregularities mainly leads to the phase and amplitude scintillations manifested as anisotropic errors under the interaction of the geomagnetic field [22], [23], [24]. There have been two types of ionospheric scintillation artifacts observed in present L-band low-Earth-orbit (LEO) SAR images. The first type refers to the artifact of amplitude stripes originated from amplitude scintillation, which has been frequently observed in the equatorial nighttime PALSAR and PALSAR-2 acquisitions [24], [25], [26], [27], [28]. It was reported that 14% of the surveyed PALSAR acquisitions and 74% of the surveyed days suffered visible amplitude stripes across the South American continent during October 2010 [24]. The stripes' morphology and heading are dependent on the observation geometry and geomagnetic field; the imaging and interferometric performances are degraded as the stripe heading angle increases [24], [29]. The radar cross-section (RCS) and the contrast of image are enhanced by the amplitude stripes [25]. The second type refers to the artifact of azimuth defocusing due to the within-aperture decorrelation induced by phase scintillation [10], [11], [12], [22], [23], [24], [30], [31], [32], [33]. Some of the PALSAR-2 spotlight images acquired in the Ascension Island during the scintillation season were seriously degraded in azimuth resolution [34], [35], [36], [37].

As the GEO SAR is broadly concerned, some researchers focused on the ionospheric scintillation effects on its

Manuscript received 12 August 2023; revised 7 October 2023; accepted 28 October 2023. Date of publication 6 November 2023; date of current version 4 December 2023. This work was supported in part by the National Natural Science Foundation of China under Grant 62101568, and in part by the Scientific Research Program of the National University of Defense Technology under Grant ZK21-06. (Corresponding author: Yifei Ji.)

Feixiang Tang, Yifei Ji, Yongsheng Zhang, Zhen Dong, and Zhaokai Wang are with the College of Electronic Science and Technology, National University of Defense Technology (NUDT), Changsha 410073, China (e-mail: tfx@nudt.edu.cn; jyfnudt@163.com; zyscn@163.com; dongzhen@vip.sina.com; wangzhaokai@nudt.edu.cn).

Qingjun Zhang, Bingji Zhao, and Heli Gao are with the Institute of Remote Sensing Satellite, China Academy of Space Technology, Beijing 100194, China (e-mail: ztzhangqj@163.com; zachary\_zbj@163.com; gaoheli\_cast@163.com).

Digital Object Identifier 10.1109/JSTARS.2023.3330752

imaging [38], [39], [40], [41], [42], [43], [44]. Li et al. [38] and Dong et al. [39] carried out simulation analysis by means of the ionospheric scintillation measurements from the GPS receiver. Hu et al. [40] quantitatively evaluated the impacts of phase and amplitude scintillations on the azimuth resolution, integrated-side-lobe ratio (ISLR) and peak-to-side-lobe ratio (PSLR). All these imaging indexes are related to the normalized standard deviation of intensity scintillation and the standard deviation of phase scintillation. The results indicated that the weak and moderate scintillation could only deteriorate the ISLR rather than the resolution and PSLR [40]. Wang et al. [41] explored the compensation of phase and amplitude scintillation in L-band GEO SAR images, based on the minimized entropy autofocus. Ji et al. [42] presented a numerical analytical model of the generalized ambiguous function (GAF) to describe the effects of drifting ionospheric irregularities on L-band GEO SAR imaging, which showed that the irregularity drifting cannot be neglected for GEO SAR because its scanning velocity of ionospheric penetration points (IPPs) is much slower than that of the LEO SAR. Ji et al. [43] also evaluated the impacts of drifting and anisotropic ionospheric irregularities on L-band GEO SAR azimuth resolution, PSLR, ISLR, peak power loss, and peak location using Monte-Carlo simulations as to the point-target scene. However, the 1D drifting PS line along azimuth is implemented in the simulations of the point-target scene without range variation. The spatial variation of scintillation phase and amplitude histories across the ultralarge extended-target scene and the interferometric decorrelation are particularly investigated, but in the case without drifting effects. Furthermore, Ji et al. [44] put forward a reverse backprojection approach to modulate the two-way scintillation transfer function (STF) on L-band GEO SAR signals with high precision and excellent efficiency, which was applied to the simulation of a large-sized image scene.

Even though the effects of drifting ionospheric irregularities on L-band GEO SAR imaging have been investigated for the point-target, the simulation for extended-target scene has rarely been involved, which is important for simulating ionospheric scintillation artifacts in future L-band GEO SAR imagery and interferometry products. In this article, a drifting ionospheric scintillation simulator (DISS) is proposed for generating L-band GEO SAR raw data affected by the drifting ionospheric scintillation phase and amplitude errors. This simulator does not need to produce a spatial-2D and temporal STF occupying a large amount of computing resources, but a static spatial-2D STF. The IPPs drifting offset indexer is skillfully designed for the echo generator to convert the temporal variation of drifting errors to the spatial variation of IPPs. The effectiveness of the DISS is validated by simulation experiments of the point-target and extended-target scenes. The imaging and interferometric performance of L-band GEO SAR is deeply investigated using DISS by comparison with that of existent L-band LEO SAR systems.

The rest of this article is organized as follows. The wave scintillation theory is briefly introduced in Section II. In Section III, the DISS procedure is discussed in detail, based on the geometric model of GEO SAR signal propagation in drifting ionospheric irregularities. Simulation experiments for confirming the

validity of the DISS are conducted in Section IV. Finally, Section V concludes this article.

## II. WAVE SCINTILLATION THEORY

### A. Phase Screen (PS) Theory

According to the PS theory, the ionospheric irregularities can be generally regarded as a thin screen changing the phase of trans-ionospheric signals under the condition of weak scatter. The phase error introduced by the PS can be modeled as [45]

$$\delta\phi_0 = -r_e\lambda \cdot \int \delta N_e dl \quad (1)$$

where  $r_e$  is the classical electron radius,  $\lambda$  is the wavelength,  $\delta N_e$  is the fluctuating part of the electron density, and  $dl$  is the differential along the propagation path  $l$ . After passing through the ionosphere, the SAR signals with phase errors continue to propagate in free space and mutually interfere, which generates a diffraction pattern on the front-wave surface. This procedure can be described by the Kirchhoff diffraction principle, and the wave electric field is presented by [45]

$$\xi(\boldsymbol{\rho}) = \frac{jk}{2\pi d_R} \iint \exp \left\{ j \left[ \delta\phi_0(\boldsymbol{\rho}') - \frac{k}{2d_R} |\boldsymbol{\rho} - \boldsymbol{\rho}'|^2 \right] \right\} d^2\boldsymbol{\rho}' \quad (2)$$

where  $k = 2\pi/\lambda$  is the wavenumber,  $\boldsymbol{\rho}$  or  $\boldsymbol{\rho}'$  signifies the 2-D spatial vector,  $d_R = H_1 H_2 \sec\theta / (H_1 + H_2)$  signifies the modification factor for the spherical wave propagation [26],  $H_1$  is the PS height,  $H_2$  is the vertical distance from the PS to the wave source, and  $\theta$  is the incident angle at the PS height. The STF in (2) can be also derived by the Helmholtz equation, which is presented by [26]

$$\xi(\boldsymbol{\rho}) = \exp \{ \alpha(\boldsymbol{\rho}) + j\delta\phi(\boldsymbol{\rho}) \} \quad (3)$$

where  $\exp\{\alpha(\boldsymbol{\rho})\}$  refers to the scintillation amplitude error imposed by the diffraction procedure, and  $\delta\phi(\boldsymbol{\rho})$  refers to the final phase perturbations of the one-way STF at the wave-front surface. In fact, the diffraction procedure motivated by the PS scintillation phase error (PS-SPE) changes the phase structure to the STF-SPE and induces the amplitude error [26].

### B. Spectrum Mechanism

The spectrum mechanism is to describe the phase fluctuation imposed by ionospheric irregularities. The spectrum density function (SDF) in the 2D wavenumber domain with regard to the PS can be expressed as [45]

$$S_{\delta\phi_0}(\kappa_x, \kappa_y) = \frac{r_e^2 \lambda^2 a b \sec^2\theta \cdot C_k L (2\pi/1000)^{p+1}}{[\kappa_0^2 + (A_1 \kappa_x^2 + A_2 \kappa_x \kappa_y + A_3 \kappa_y^2)]^{(p+1)/2}} \quad (4)$$

where  $C_k L$  signifies the vertical integrated turbulence strength,  $p$  is the power spectrum index,  $\kappa_0 = 2\pi/L_0$  is the wavenumber cut-off with regard to the outer scale  $L_0$ ,  $\kappa_x, \kappa_y$  signify the 2D spatial wavenumber with regard to the spatial separation  $\rho_x, \rho_y$ , and  $a, b$  signify the two anisotropic axis scales. The coefficients of  $A_1, A_2, A_3$  are dependent on the incident angle  $\theta$ , squint angle  $\varphi$ , two anisotropic axis scales  $a, b$ , geomagnetic heading angle

$\delta_B$ , geomagnetic inclination angle  $\theta_B$ , and third rotation angle  $\gamma_B$ . The interested readers can consult [43] for more detail.

The SDFs of the phase and amplitude scintillations imposed by the diffraction can be presented as [36] and [37]

$$S_{\delta\phi}(\kappa_x, \kappa_y) = S_{\delta\phi_0}(\kappa_x, \kappa_y) \cdot \cos^2 \left[ \frac{(\kappa_x^2 + \kappa_y^2) d_R}{2k} \right] \quad (5)$$

$$S_{\alpha}(\kappa_x, \kappa_y) = S_{\delta\phi_0}(\kappa_x, \kappa_y) \cdot \sin^2 \left[ \frac{(\kappa_x^2 + \kappa_y^2) d_R}{2k} \right]. \quad (6)$$

According to (5), the diffraction merely changes the high-frequency components because of the interaction of the square cosinusoid, and thus will not significantly change the PS-SPE, which indicates that the PS-SPE approximates to the STF-SPE [31], [36], [37]. According to (6), the SDF of the logarithmic amplitude is modulated by the square sinusoid, and therefore the spatial structures larger than the first Fresnel cutting scale become dominant in the amplitude pattern, which makes the high-frequency components more significant and contributes to the bright-dark amplitude stripes [47].

### C. Drifting Ionospheric Irregularities

The above spectrum mechanism gives a good description of the hypothetical case of static ionospheric irregularities, which is reasonable for existent LEO SAR systems due to the fact that the IPP scanning velocity is much higher than the drifting velocity of ionospheric irregularities. Nevertheless, the drifting of equatorial ionospheric irregularities cannot be neglected any longer for future GEO SAR system due to the much lower IPP scanning velocity [42], and this conclusion will be confirmed in Section II. For the moment, if we take only the drifting of the ionospheric irregularities into account and neglect the temporal structural decaying of the overall irregularities, the resultant PS-SPE then satisfies [48], [49]

$$\delta\phi_0(t + \Delta t, \rho) = \delta\phi_0(t, \rho - \mathbf{v}_i \Delta t) \quad (7)$$

where  $\mathbf{v}_i$  is the horizontal drifting velocity vector of ionospheric irregularities, which is perpendicular to the local electric and geomagnetic field [27]. A field that satisfies (7) is known as the ‘‘frozen field’’ for such a field is convected with  $\mathbf{v}_i$  as if it was frozen [48], [49]. According to most ionospheric scintillation observation results in Hainan, China and in Jicamarca, Peru, the typical equatorial ionospheric irregularities were drifting with an absolute velocity from 0 to 300 m/s, and the drifting orientation tended to be westward at daytime and eastward at nighttime [50], [51]. Furthermore, it was reported that the ionospheric irregularities near the equator tracked toward the geomagnetic east with a velocity of about 100 m/s [52].

### D. Numerical Realization of PS and STF

The numerical realization of the static PS is motivated by a random process that the Hermitian Gaussian white noise with the zero mean and unit variance passes through a linear system with the certain power spectrum characteristics. This random process can be realized by the numerical operation presented

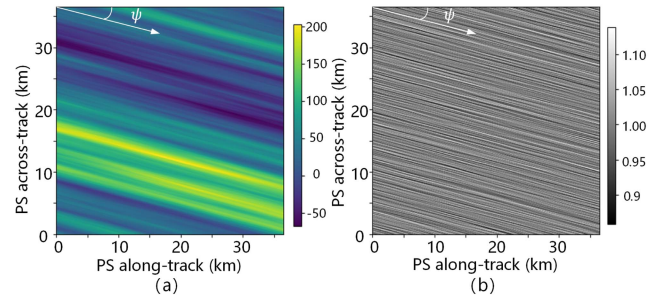


Fig. 1. Example of the PS and STF simulation for the L-band (1.25 GHz) system on condition of  $C_k L = 10^{34}$ ,  $p = 3$ ,  $a : b = 50 : 1$ ,  $L_o = 10$  km,  $\theta = 30$  deg,  $\varphi = 90$  deg,  $\delta_B = 30$  deg,  $\theta_B = 15$  deg,  $\gamma_B = 0$  deg. (a) 2-D phase error (unit: deg). (b) 2-D normalized amplitude scintillation.

as [43]

$$\delta\phi_0(\rho) = \frac{MN}{2\pi} \cdot \text{IFFT}_2 \left\{ \frac{g_1 + jg_2}{\sqrt{2}} \sqrt{S_{\delta\phi_0}(\kappa) \cdot \Delta\kappa_x \Delta\kappa_y} \right\} \quad (8)$$

where  $\text{IFT}_2(\cdot)$  refers to the 2-D inverse fast fourier transform (FFT),  $M$  and  $N$  are the along-track and across-track sampling number,  $\Delta\kappa_x$  and  $\Delta\kappa_y$  are the wavenumber sampling interval in two directions, respectively, and  $g_1$  and  $g_2$  signify mutually uncorrelated and the real and imaginary parts of the complex Gaussian noise in the wavenumber domain, respectively. The split-step approach based on the Helmholtz equation is used to derive the STF from the PS, which proves to be equivalent to the Kirchhoff’s formula presented in (2), and interested readers can consult [43] for more details. The numerical STF can be realized by [26]

$$\xi(\rho) = \text{IFFT}_2 \left\{ \text{FFT}_2 \left\{ \exp[j\delta\phi_0(\rho)] \right\} \cdot \exp \left( \frac{j d_R}{2k} \kappa^2 \right) \right\} \quad (9)$$

where  $\text{FFT}_2(\cdot)$  refers to the 2-D FFT.

Fig. 1 presents an example of the PS and STF simulation in case of the typical equatorial static ionospheric irregularities. The 2-D PS-SPE and amplitude error of the STF are presented in Fig. 1(a) and (b), respectively. Due to the interaction of the geomagnetic field, the actual ionospheric irregularities are anisotropic, which tend to be rod-like ( $a \gg b$ ) near the equator and sheet-like ( $a \approx b$ ) in auroral areas [25]. This article addresses the equatorial case because the auroral areas are not illuminated by a typical inclined GEO SAR. On condition of  $a : b = 50 : 1$ , both the SPE and amplitude error caused by the rod-like anisotropic irregularities are elongated in one direction (see white arrows), along which the spatial correlation is the strongest. The angle between the elongation direction and the azimuth is called anisotropic elongation heading and denoted by  $\psi$ , which is mainly dependent on  $\theta_B$ ,  $\delta_B$ ,  $\theta$  and  $\varphi$  and has a significant impact on SAR imaging [24], [36], [37], [43].

Above presents a description of the numerical realization of the static PS and STF. Because the temporal variation of the drifting PS is only involved in a shifting process, the drifting PS can be numerically realized by substituting the spectrum SDF in (8) by  $S_{\delta\phi_0}(\kappa) \cdot \exp(j\kappa \cdot \mathbf{v}_i t)$  [48], [49]. In practice, a

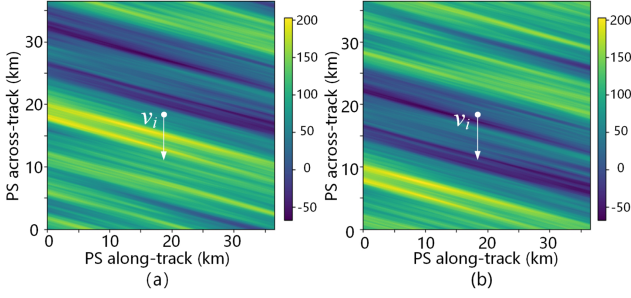


Fig. 2. Example of the drifting PS simulation on condition of  $C_k L = 10^{34}$ ,  $p = 3$ ,  $a : b = 50 : 1$ ,  $L_o = 10$  km,  $\theta = 30$  deg,  $\varphi = 90$  deg,  $\delta_B = 30$  deg,  $\theta_B = 15$  deg,  $\gamma_B = 0$  deg,  $v_i = 100$  m/s. The drifting direction is just in PS across-track. (a) 2-D phase error (unit: deg) at  $t = 0$  s. (b) 2-D phase error (unit: deg) at  $t = 100$  s.

large-size PS is generated to cover the whole ionospheric structure during the given time and to avoid the circumferential shift of the FFT by observing in a fix window. Fig. 2 presents an example of the drifting PS during a temporal interval of 100 s, which is of the similar order of magnitude compared with the synthetic aperture time of GEO SAR. The ionospheric irregularities drift in PS across track with a velocity of 100 m/s. In this case, the ionospheric PS drifts about 10 kilometers on the whole, which causes significant temporal decorrelation in azimuth and thereby has a significant impact on GEO SAR imaging.

### III. METHODOLOGY

Based on the simulated PS and STF imposed by the static ionospheric irregularities, the ionospheric scintillation impacts on LEO SAR can be easily simulated by mapping the STF to each azimuth echo according to the IPP coordinate [43], [44]. Nevertheless, the drifting ionospheric irregularities should be considered for GEO SAR, and the echo simulation requires to produce the temporal-varying and 2D-spatial-distributed PS and STF (3D in total), which is hardly accomplished because it consumes a large amount of computing resources. Given that the overall structure of the ionospheric irregularities maintains stability during drifting, the STF for each azimuth echo can be indirectly indexed according to the effective IPP, which greatly frees computing resources and improves simulation efficiency because only 2D spatially distributed STF is involved. In this section, the model of the trans-ionospheric signal of GEO SAR along with the anisotropic and drifting geometry is introduced, based on which a novel simulator for simulating the effects of the drifting and anisotropic ionospheric irregularities on GEO SAR is devised and discussed.

#### A. Trans-Ionospheric GEO SAR Signal Model

Fig. 3 illustrates the geometry of GEO SAR signal propagation across the equatorial anisotropic and drifting ionospheric irregularities. As shown in Fig. 3,  $\theta_d$  is the down-look angle,  $R_0$  is the center slant range,  $L_s$  is the synthetic aperture length of GEO SAR with regard to the synthetic aperture time  $T_s$ ,  $\psi$  denotes the anisotropic elongation angle,  $v_p$  signifies the IPP

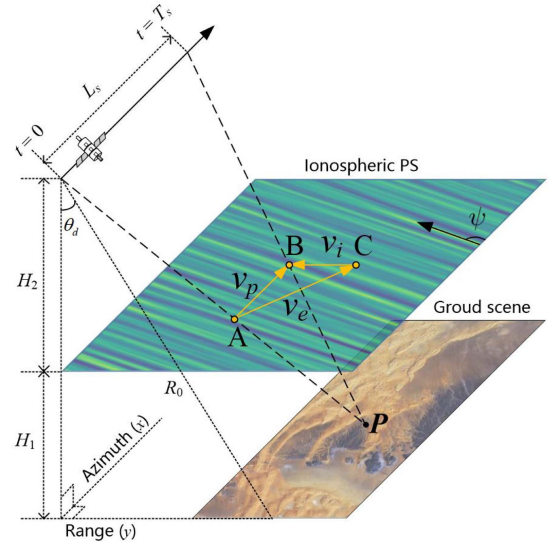


Fig. 3. Geometry of trans-ionospheric propagation of GEO SAR.

scanning velocity in along-track, and  $v_e = v_p - v_i$  signifies the effective velocity between the IPP scanning velocity  $v_p$  and the horizontal structural drifting velocity  $v_i$ . As to the point scatterer  $P$ , the IPP within the synthetic aperture tracks from A to B with the velocity  $v_p$ . In GEO SAR signal acquisition, the radio signals propagate through the ionosphere by twice, and the down and up STFs can be generally considered to be equivalent because the ionospheric drifting distance during the separation between upward and downward transitions is well below the inner-size [42], [43]. Hence, the L-band GEO SAR signal in presence of the anisotropic and drifting ionospheric irregularities can be expressed by the convolution of reflection coefficient of ground scene and the SAR impulse response function (IRF) [43]

$$s_0(\tau, \eta) = \int \sigma(\mathbf{P}) h(\tau, \eta; \mathbf{P}) d\mathbf{P} \quad (10)$$

$$h(\tau, \eta; \mathbf{P}) = h_0(\tau, \eta; \mathbf{P}) \times \zeta_{\mathbf{P}}^2(\eta; \rho_x, \rho_y)$$

$$= w_r \left[ \tau - \frac{2R_{\mathbf{P}}(\eta)}{c} \right] \exp \left\{ -j\pi K_r \left[ \tau - \frac{2R_{\mathbf{P}}(\eta)}{c} \right]^2 \right\}$$

$$\cdot w_a(\eta - \eta_{\mathbf{P}}) \exp \left[ -\frac{j4\pi R_{\mathbf{P}}(\eta)}{\lambda_c} \right] \times \zeta_{\mathbf{P}}^2(\eta; \rho_x, \rho_y) \quad (11)$$

where  $\tau$  and  $\eta$  refer to the fast and slow time, respectively,  $\sigma(\mathbf{P})$  signifies the scatterer reflectivity of  $\mathbf{P}$ ,  $h_0(\tau, \eta; \mathbf{P})$  is the ideal IRF of  $\mathbf{P}$ ,  $h(\tau, \eta; \mathbf{P})$  is the scintillation-influenced IRF,  $\zeta_{\mathbf{P}}^2(\cdot)$  is the two-way anisotropic STF of  $\mathbf{P}$  versus the azimuth time and IPP coordinate  $(\rho_x, \rho_y)$ ,  $w_r$  is the range window,  $R_{\mathbf{P}}(\eta)$  is the slant range of  $\mathbf{P}$ ,  $c$  is the light velocity in the vacuum,  $K_r$  is the slope of linear frequency modulation in range,  $w_a$  is the azimuth window,  $\eta_{\mathbf{P}}$  is the center azimuth time of  $\mathbf{P}$ , and  $\lambda_c$  is the wavelength with regard to the carrier frequency. Note that, in the consideration of an empirical height of the ionosphere  $H_1 = 350$  km, the small interval between twice penetration can be calculated to  $\Delta\eta = 2H_1/c \approx 2.33$  ms. Thus, the down and

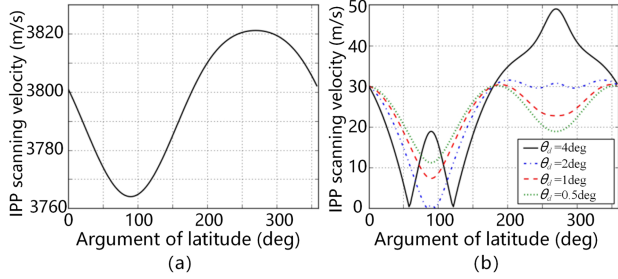


Fig. 4. IPP scanning velocity of the L-band (1.25 GHz) spaceborne SAR systems. (a) LEO SAR with  $H_1 = 350$  km,  $H_1 + H_2 = 700$  km. (b) GEO SAR with a typical inclined orbit of 60 deg and  $H_1 = 350$  km,  $H_1 + H_2 = 35786$  km.

up STFs have  $\zeta_{\mathbf{P}}^{\text{up}}(\eta; \rho_x, \rho_y) \cdot \zeta_{\mathbf{P}}^{\text{down}}(\eta + \Delta\eta; \rho_x + v_{ix}\Delta\eta, \rho_y + v_{iy}\Delta\eta) \approx \zeta_{\mathbf{P}}^2(\eta; \rho_x, \rho_y)$ .

According to (11), the IRF is modulated by the square STFs according to the azimuth time and IPP coordinate, and the IPP coordinate can be determined by the satellite and scene pixel location. During the synthetic aperture time, the ionospheric PS and STF is varying due to the drifting. Considering that the overall structure of the STF is stable, the effective IPP actually drifts from A to C (see Fig. 3). Therefore, the impacts of the anisotropic and drifting ionospheric irregularities involved in the spatio-temporal STF are comprehensively integrated in the GEO SAR signal model, which has an important impact on L-band GEO SAR imaging and interferometry.

### B. Anisotropic and Drifting Geometry of Equatorial Ionospheric Irregularities for GEO SAR

The effective drifting velocity vector is an important factor that describes the geometry between the SAR satellite tracking and drifting irregularities, and it is related to the IPP scanning velocity  $v_p$  and the horizontal structural drifting velocity  $v_i$ . The IPP of  $\mathbf{P}$  tracks from A to B during the synthetic aperture time, and thus  $v_p$  can be calculated by

$$v_p = \frac{L_s^i}{T_s} \approx \frac{\theta_s R_0 H_1}{T_s \cdot (H_1 + H_2)} \quad (12)$$

where  $L_s^i$  is the projected synthetic aperture length at the PS height, and  $\theta_s$  is the integrated angle (see Fig. 3), which can be calculated by  $\theta_s \approx 0.443\lambda_c/\rho_a$ , where  $\rho_a$  is the designed azimuth resolution. Furthermore, due to the interaction of the Earth rotation,  $v_p$  varies from different look-down angles and different arguments of latitude. The IPP scanning velocity of LEO SAR and GEO SAR is calculated and shown in Fig. 4. A typical GEO SAR system with an orbital inclination of 60 deg is adopted. It shows that  $v_p$  of LEO SAR reaches more than 3 km/s all around the orbit, while that of GEO SAR fluctuates around 30 m/s, and is even lower than 10 m/s in some orbital positions and in case of a larger look-down angle. As a result,  $v_p$  of LEO SAR is much higher than the drifting velocity of the equatorial ionospheric irregularities with about 100 m/s. It means that the irregularity drifting can be reasonably ignored in LEO SAR for  $v_p \gg v_i$  and  $v_e \approx v_p$ , even though the slight

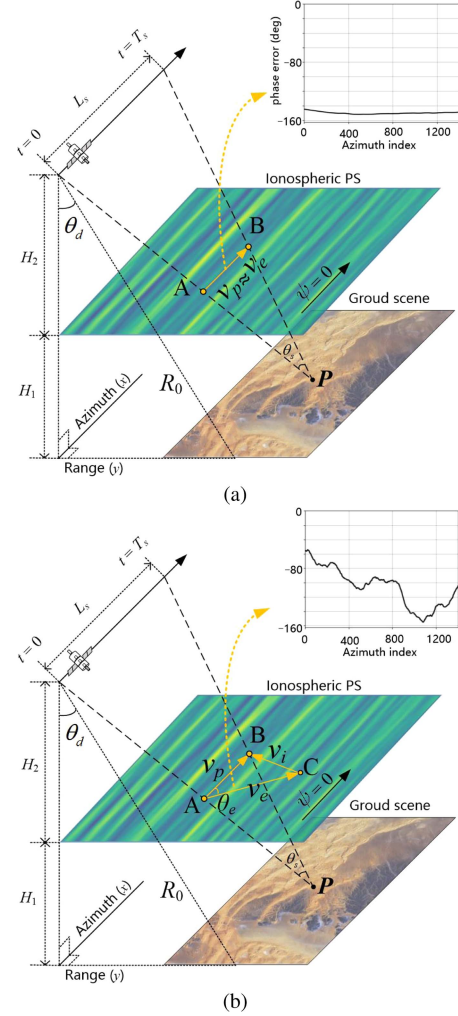


Fig. 5. Geometry of trans-ionospheric synthetic aperture imaging in case of the equatorial drifting and anisotropic ionospheric irregularities with  $\psi = 0$  deg. (a) LEO SAR. (b) GEO SAR.

drifting can be still detected from the variation of amplitude stripes in different PALSAR sublooks [27]. On the contrary,  $v_p$  of GEO SAR is comparable with the drifting velocity of the ionospheric irregularity in the equatorial areas, which makes the effect of drifting ionospheric irregularities more significant in GEO SAR.

Fig. 5 illustrates the geometry of the equatorial drifting and anisotropic ionospheric irregularities for both LEO SAR and GEO SAR systems, and the anisotropic elongation heading is artificially designed to be in along-track ( $\psi = 0$ ). As a result, the effective IPP of LEO SAR just tracks in azimuth due to  $v_e \approx v_p$ . In this case, the in-aperture scintillation phase and amplitude errors of  $\mathbf{P}$  tend to be uniform [see Fig. 5(a)], which indicates the appearance of the so-called amplitude stripes that have been frequently detected in the PALSAR and PALSAR-2 images [24], [25], [26], [27], [28]. Differing from the LEO case, the effective IPP of GEO SAR tracks off course due to the interaction of the significant  $v_i$  [see Fig. 5(b)]. The deviation angle between  $v_e$  and  $v_p$  is the effective IPP angle denoted by  $\theta_e$ . In this case, the scintillation phase and amplitude errors violently fluctuate

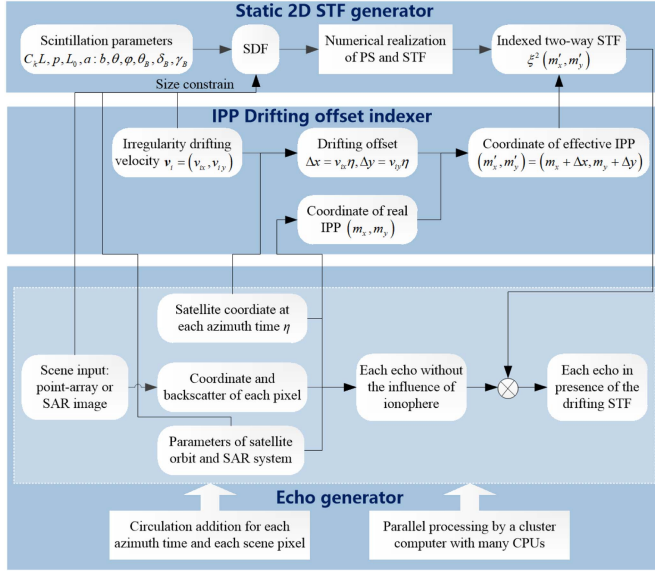


Fig. 6. Flow chart of DISS.

within the synthetic aperture of GEO SAR, which leads to the imaging distortion and the disappearance of amplitude stripes.

In previous studies on LEO SAR, the types of ionospheric scintillation artifacts proved to be determined by  $\psi$  [24], [36], [37], [43], [47]. It was concluded that when  $|\psi|$  is close to zero, the SAR images suffer from the amplitude stripes with the nice imaging quality; as  $|\psi|$  continues to rise, the artifact of amplitude stripes gradually vanish accompanied by the serious azimuth defocusing. Considering the more general case of the drifting ionospheric irregularities for both LEO SAR and GEO SAR,  $\psi - \theta_e$  becomes the crucial factor. Note that,  $\psi - \theta_e$  degenerate to the special case of LEO SAR for  $\theta_e \approx 0$ . With loss of generality, the amplitude stripes occur, and the imaging quality presents a good status, when the effective IPP nearly drifts along the anisotropic elongation heading ( $|\psi - \theta_e| \approx 0$ ). With the increase of  $|\psi - \theta_e|$ , the amplitude stripes vanish, and the azimuth imaging and interferometric coherence are seriously degraded.

### C. Procedure of DISS

In order to investigate the effects of the drifting ionospheric irregularities on L-band GEO SAR, a novel simulator, DISS, is devised. The processing procedure is shown in Fig. 6, which is mainly divided into three modules: a static 2D STF generator, an IPP drifting offset indexer, and a GEO SAR echo generator. Details are specified as follows.

In the module of the static 2D STF generator, the 2D SDF of the PS should be calculated according to (4) and based on the input ionospheric scintillation parameters. Some digitized factors need to be declared in particular. The 2D wavenumber  $\kappa_x$  and  $\kappa_y$  can be spaced by the intervals of  $2\pi/L_x$  and  $2\pi/L_y$ , respectively, where  $L_x$  and  $L_y$  represent the along-track and across-track sizes of the PS. Note that, the PS size should be large enough to entirely cover the ground scene and synthetic

aperture. Furthermore, considering the irregularity drifting, the drifting offset should be added to the PS size. Therefore,  $L_x$  and  $L_y$  should be constrained by

$$\begin{aligned} L_x &\geq \max \{L_0, L_s^i + L_a + v_{ix}T_t\} \\ L_y &\geq \max \left\{ L_0, \frac{H_2L_r}{H_1 + H_2} + v_{iy}T_t \right\} \end{aligned} \quad (13)$$

where  $L_a$  and  $L_r$  signify the azimuth and ground-range size of the observation scene,  $v_{ix}$  and  $v_{iy}$  signify the along-track and across-track velocity of the irregularity drifting, respectively,  $L_s^i$  can be calculated by  $L_s^i = H_1L_s/(H_1 + H_2)$ , and  $T_t$  is the total duration of GEO SAR acquisition. The floor level of the PS size should be larger than the outer scale for satisfying the statistical ergodicity. Then, the numerical 2D PS and STF can be produced according to (8) and (9), and all drifting IPPs are contained.

In the module of the IPP drifting indexer, it is necessary to firstly calculate the coordinate of the real IPP (see the tracking line from A to B in Figs. 3 and 4). As to the point scatterer  $P$ , the real IPP is the point, where the line from the satellite position at each azimuth time  $\eta$  to  $P$  intersects the spherical surface of the PS height, and thus its coordinate  $(m_x, m_y)$  is calculated based on the coordinate of the satellite and scene pixel and the PS height. Note that,  $(m_x, m_y)$  is also a function of  $\eta$  and  $P$  and should be calculated at each azimuth time and for each pixel. In fact,  $m_y$  only depends on the coordinates of different across-track pixels in the scene coordinate system, and the computation complexity can be lowered by using this feature. Considering that the overall structure of the drifting ionospheric irregularities keeps constant during the integrated time, the static 2D STF for the initial moment is sufficient for the echo simulation, and hence the effective IPP at the fixed STF actually tracks from A to C (see Figs. 3 and 4). The drifting offset of the IPP is  $(\Delta x, \Delta y) = (v_{ix}\eta, v_{iy}\eta)$ . Thereby, the effective IPP is calculated by

$$(m'_x, m'_y) = (m_x + v_{ix}\eta, m_y + v_{iy}\eta) \quad (14)$$

based on which the two STF for the fixed azimuth time and scene pixel can be easily indexed.

In the last module of the echo generator, a point-array or image scene is input, and the simulation principle or procedure is actually similar for both two types of scenes. Based on the satellite and SAR system parameters, each echo in absence of the ionospheric scintillation influence can be simulated at each azimuth time and for each pixel according to (11). Note that, each pixel echo should be modulated by a beam window, and the rectangular window is adopted for convenience. The pure echo is modulated by the indexed two-way STF  $\xi^2(m'_x, m'_y)$  for generating the contaminated SAR echo, which integrally contains the impacts of the anisotropic and drifting ionospheric irregularities. Circulation addition for each azimuth time and each scene pixel is then performed to produce the SAR echo of the whole scene, which can be easily realized for the point-array scene due to a small number of effective pixels. However, it is difficult to simulate the scintillation-influenced GEO SAR echo for the image scene, which is actually a dense point-array scene comprising a large number of effective pixels. Therefore, a triple nested for-loop structure for azimuth time, and azimuth

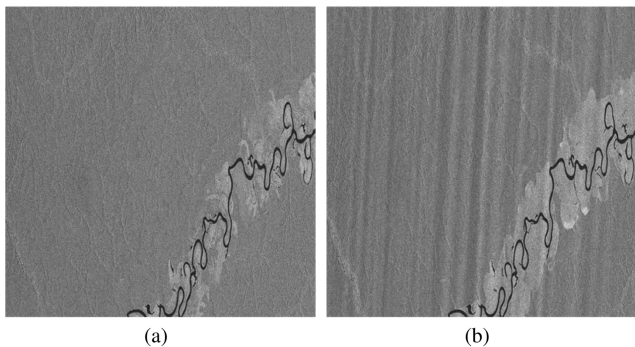


Fig. 7. ALOS PALSAR images (truncated). (a) Scene ID: ALPSRP102117100 acquired in the Amazon Forest on December 25, 2007 in absence of amplitude stripes. (b) Scene ID: ALPSRP115537100 acquired in the same area on March 28, 2008 in presence of amplitude stripes.

and range pixels of the image scene is involved, which leads to the low processing efficiency. Two strategies can be adopted to improve the efficiency. On one hand, the echo at each azimuth time can be simultaneously produced for the pixels in the same range bin, which can transform the triple nested for-loop to a nearly double nested for-loop project. On the other hand, the parallel processing by a cluster computer with a number of CPUs is beneficial to hugely promote the simulation efficiency, especially for the simulation of a large-size image scene.

Compared with the traditional echo simulation approach in [43] and [44], the biggest difference of the DISS is the design of the IPP drifting offset indexer, which skillfully considers the drifting characteristic of ionospheric irregularities. Next, some simulation experiments will be conducted to validate the DISS effectiveness and to examine the impacts of the drifting and anisotropic ionospheric irregularities on L-band GEO SAR.

#### IV. VALIDATION

The methodology of the DISS has been introduced above in detail. To validate the effectiveness of the DISS, the simulation experiments of the point-target and extended-target scenes will be implemented in this section. The point-target simulation is to study the different impacts of the drifting and anisotropic ionospheric irregularities on L-band LEO SAR and GEO SAR azimuth imaging, and the extended-target simulation derived from an ALOS PALSAR image in the absence of amplitude stripes is to investigate the ionospheric artifacts in GEO SAR images and interferograms.

##### A. Data and Parameter Declaration

Fig. 7 shows two ALOS PALSAR real images (truncated) acquired in the Amazon Forest. One shown in Fig. 7(a) refers to the case of the quiet ionosphere and will be used for the extended-target simulation. Another shown in Fig. 7(b) suffers from significant amplitude stripes and will be a comparison with the following simulated L-band GEO SAR images. The anisotropic elongation angle is estimated to be about  $-4$  deg by using the approach in [28], which is a typical setting in the following simulation.

TABLE I  
SYSTEM PARAMETERS OF L-BAND LEO SAR AND GEO SAR

Parameters	LEO SAR	GEO SAR	Unit
Radar altitude	700	35793	km
Carrier frequency	1.27	1.27	GHz
System bandwidth	28	28	MHz
Integrated time $T_s$	2.23	253.57	s
IPP velocity $v_p$	2.55	0.02	km/s

TABLE II  
IONOSPHERIC PARAMETERS

Parameters	Specification	Unit
Ionospheric height $H_1$	230	km
Outer scale $L_o$	10	km
Spectrum index $p$	3	-
Integrated turbulence strength $C_k L$	$1 \times 10^{34}$	-
Anisotropic scale ratio $a : b$	50 : 1	-
Anisotropic elongation angle $\psi$	$-4, 30$	deg
Drifting velocity $v_i$	100	m/s
Geomagnetic heading angle $\delta_B$	$-4, 30$	deg
Geomagnetic inclination angle $\theta_B$	0	deg
Third rotation angle $\gamma_B$	0	deg

The system parameters of L-band LEO SAR and GEO SAR are summarized in Table I. The satellite and system parameters of the ALOS PALSAR are considered to be the typical L-band LEO SAR and used for simulation. The conceptual GEO SAR is similar to moving an LEO SAR satellite to a typical inclined geosynchronous orbit. The parameters of anisotropic and drifting ionospheric irregularities in the equatorial areas used for simulation are listed in Table II. An estimated value of the equivalent height of the ionospheric PS is set to be 230 km, which is estimated from the ALOS-2 PALSAR-2 real images [37]. The IPP scanning velocity  $v_p$  of GEO SAR and LEO SAR can be calculated to the value about 0.02 km/s and 2.55 km/s according to (12), respectively. A highly turbulent case of  $C_k L = 10^{34}$ ,  $p = 3$ ,  $L_o = 10$  km with a rod-like structure ( $a : b = 50 : 1$ ,  $\psi = -4$  deg or 30 deg) in the equatorial areas will be considered in the following simulations. As mentioned in Section II, the velocity of ionospheric irregularities is set as 100 m/s, which is also a typical value of equatorial ionospheric irregularities measured in [50], [51].

##### B. Point-Target Simulation

Fig. 8 presents the point-target simulation results of LEO SAR and GEO SAR. The top row refers to the anisotropic PS and drifting geometry, the middle refers to the contaminated echo amplitude, and the bottom refers to the azimuth-imaging profiles of the Monte-Carlo simulation and average alongside the uncontaminated azimuth profile.

In case of  $\psi = -4$  deg, we assume that the ionospheric PS drifts along the across-track with the velocity of 100 m/s, and thus  $\theta_e$  can be calculated to be  $-54$  deg for GEO SAR and nearly 0 deg for LEO SAR, respectively. Thereby, it has  $|\psi - \theta_e| = 50$  deg for GEO SAR and  $|\psi - \theta_e| = 4$  deg for LEO SAR. The echo amplitude of GEO SAR is presented with more bright-dark stripes than LEO SAR. As to the azimuth profile of point-target imaging, the azimuth performance of LEO SAR are much better

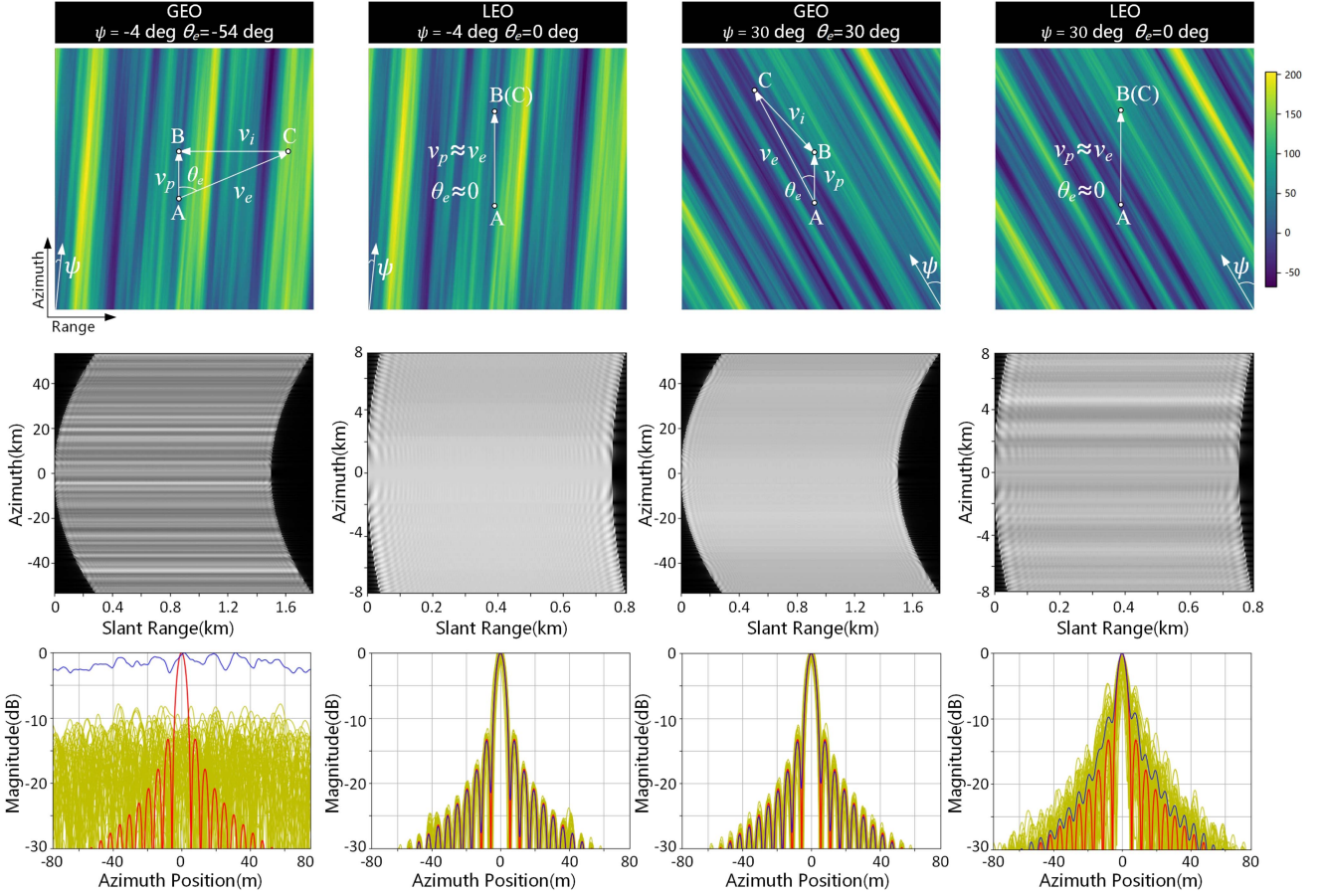


Fig. 8. Point-target simulation results. The anisotropic PS and drifting geometry (top); contaminated echo amplitude (middle); azimuth profiles (bottom) of the Monte-Carlo simulation (50 times, yellow lines) and average (blue lines) alongside the ideal azimuth profile (red lines).

than GEO SAR. Compared with the ideal azimuth profile (red line), the azimuth performance of GEO SAR (yellow lines) suffers from the severe azimuth decorrelation with regard to the deteriorated azimuth resolution, PSLR, ISLR, peak power loss and peak location. As to the GEO SAR, the IPP scanning velocity  $v_p = 0.02$  km/s is of the similar order of magnitude compared with the drifting velocity  $v_i = 100$  m/s. Hence, the heading of effective track line of GEO SAR is more deviating from the anisotropic extension angle with  $|\psi - \theta_e| = 50$  deg. The phase errors are more turbulent within the synthetic aperture like the case shown in Fig. 5(b). This means that more random scintillation phase and amplitude errors are added to the GEO SAR signals, and azimuth decorrelation magnifies at each satellite point as to the large deviation. The bright-dark stripes of the echo amplitude indicates the severe amplitude decorrelation of the GEO SAR. As to the LEO SAR, the IPP scanning velocity  $v_p = 2.55$  km/s is much faster than the drifting velocity  $v_i = 100$  m/s. Thus, the effective track line is almost along the anisotropic extension heading because of neglecting the effects of drifting with a small deviation  $|\psi - \theta_e| \approx 4$  deg. The signals of LEO SAR are modulated by the highly correlated STFs, which is almost along the anisotropic extension heading like the case shown in Fig. 5(a) with a uniform scintillation phase and amplitude errors. The echo amplitude of LEO SAR is

fluctuating more gently in azimuth, and the imaging performance of 50 times Monte-Carlo point-target in azimuth profile are highly confirming to the ideal azimuth profile in red.

But on the condition of  $\psi = 30$  deg,  $\theta_e$  is designed to the value of 30 deg for GEO SAR, which means that  $|\psi - \theta_e| = 0$  deg. As to the LEO SAR,  $\theta_e$  approximates 0 deg with the same reason that neglects the effects of drifting irregularities. Thus,  $|\psi - \theta_e| = 30$  deg for LEO SAR. On the contrary, the echo amplitude of LEO SAR is presented with more bright-dark stripes than GEO SAR, and the azimuth performance of GEO SAR are much better than LEO SAR as to the azimuth profile. The azimuth performance of LEO SAR suffers from the more severe azimuth decorrelation. On this anisotropic condition, the LEO SAR echo are affected by the violently fluctuating scintillation phase and amplitude errors.

To sum up, the deviation  $|\psi - \theta_e|$  increases, the more bright-dark stripes appears on the echo amplitude and azimuth imaging performance degrades for the point-target imaging. As to the LEO SAR, the deviation is mostly dominated by the anisotropic extension angle  $\psi$  because of neglecting the effects of drifting and the special case of  $v_p \gg v_i$ ,  $v_e \approx v_p$  and  $\theta_e \approx 0$ . Thus, the scintillation phase and amplitude errors can violently fluctuate within the synthetic aperture in LEO SAR with a large  $|\psi|$ . Note that, as to the GEO SAR, the deviation  $|\psi - \theta_e|$  is mostly



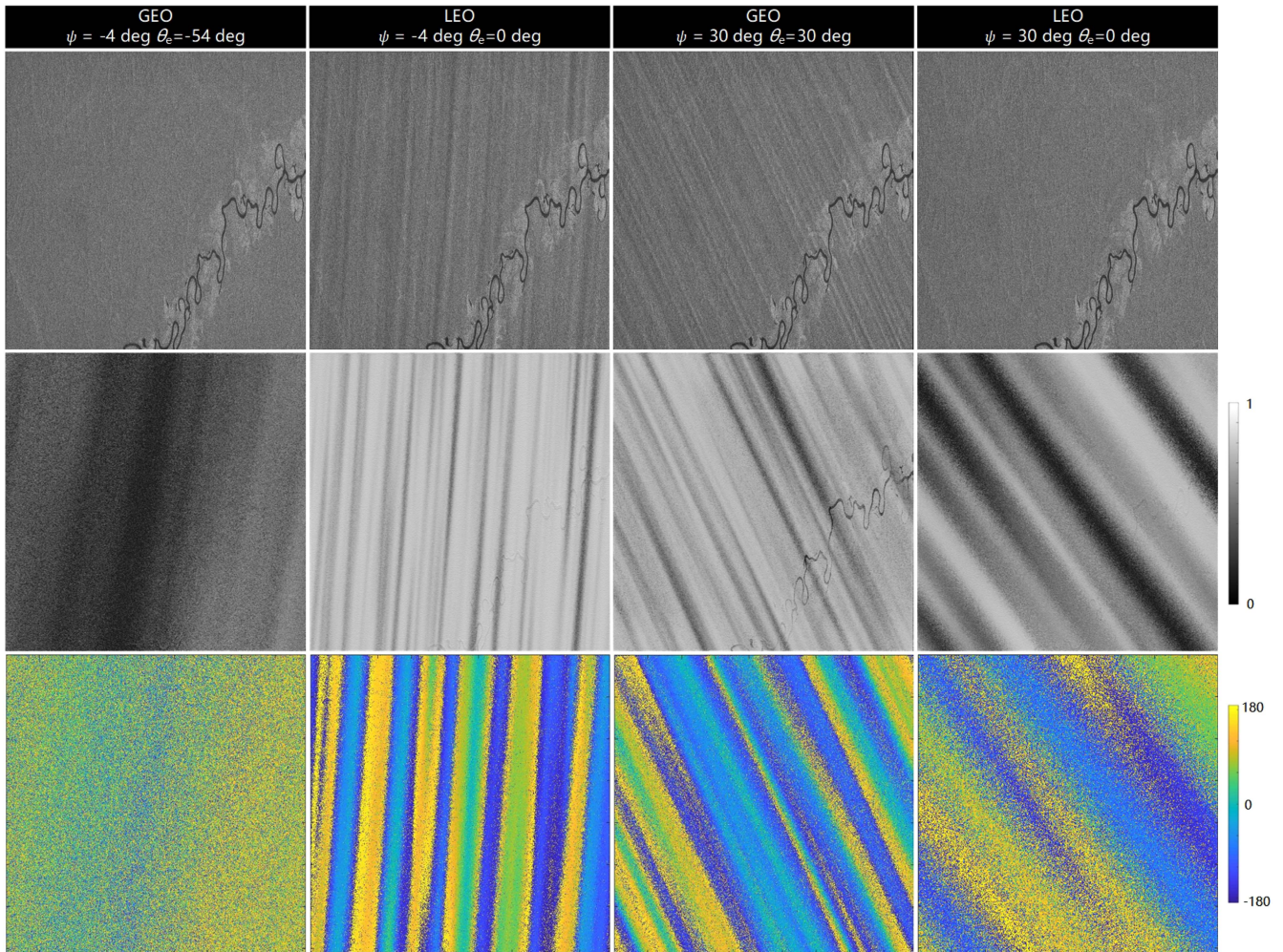


Fig. 9. Extended-target simulation on the ionospheric conditions of Fig. 8. Power images (top), complex coherent coefficient (middle) and wrapped interferometric phase error (bottom).

dependent to both the effects of drifting ionospheric irregularities and the anisotropic extension heading with the comparable weight, because the IPP scanning velocity of GEO SAR has the similar magnitude with the drifting velocity. Thus, the extended-target imaging of GEO SAR can be significantly different to LEO SAR on the two effects.

### C. Extended-Target Simulation

In the extended-target simulation, the coherent coefficient and InSAR phase error are performed to investigate the InSAR performance contaminated by the effects of drifting ionospheric irregularities. The zero-baseline interferometric process is applied according to the pure and contaminated SAR images. Fig. 9 illustrates four groups of extended-target simulation results on the ionospheric condition of Fig. 8, respectively. The top row refers to the power imaging results of extended-target, the middle refers to the complex coherent coefficient, and the bottom refers to the InSAR phase error.

In case of  $\psi = -4$  deg, the terrain details with regard to the high-frequency components disappear and amplitude stripes

vanish in the GEO SAR images, compared with Fig. 7(a). It is severely deteriorated as to the GEO-InSAR coherence in the case of  $|\psi - \theta_e| = 50$  deg. There is a diffused stripe pattern in the decorrelation structure, which has a more inclined elongation direction because of the effects of drifting irregularities. But the remarkable amplitude stripes come forth in the LEO SAR images, which is similar to the PALSAR real image in Fig. 7(b). Besides, there is high correlation along the stripe direction both in the LEO-InSAR coherence and phase map because of a small deviation  $|\psi - \theta_e| \approx 4$  deg. On the condition of  $\psi = 30$  deg, there are remarkable and dense amplitude stripes in the GEO SAR images. The high correlation is consistent to the elongation direction both in the GEO-InSAR coherence and phase map, because the effective track line is along the anisotropic extension heading with  $|\psi - \theta_e| = 0$  deg. However, the amplitude stripes can be vanishing in the case of  $\psi = 30$  deg on LEO SAR images. Note that,  $\psi = 30$  deg is big enough to dissipate the amplitude stripes [24], [27], [43]. The pattern of InSAR coherence are ambiguous, and more phase perturbations or called speckle-like phase dots appear in the LEO-InSAR phase maps.

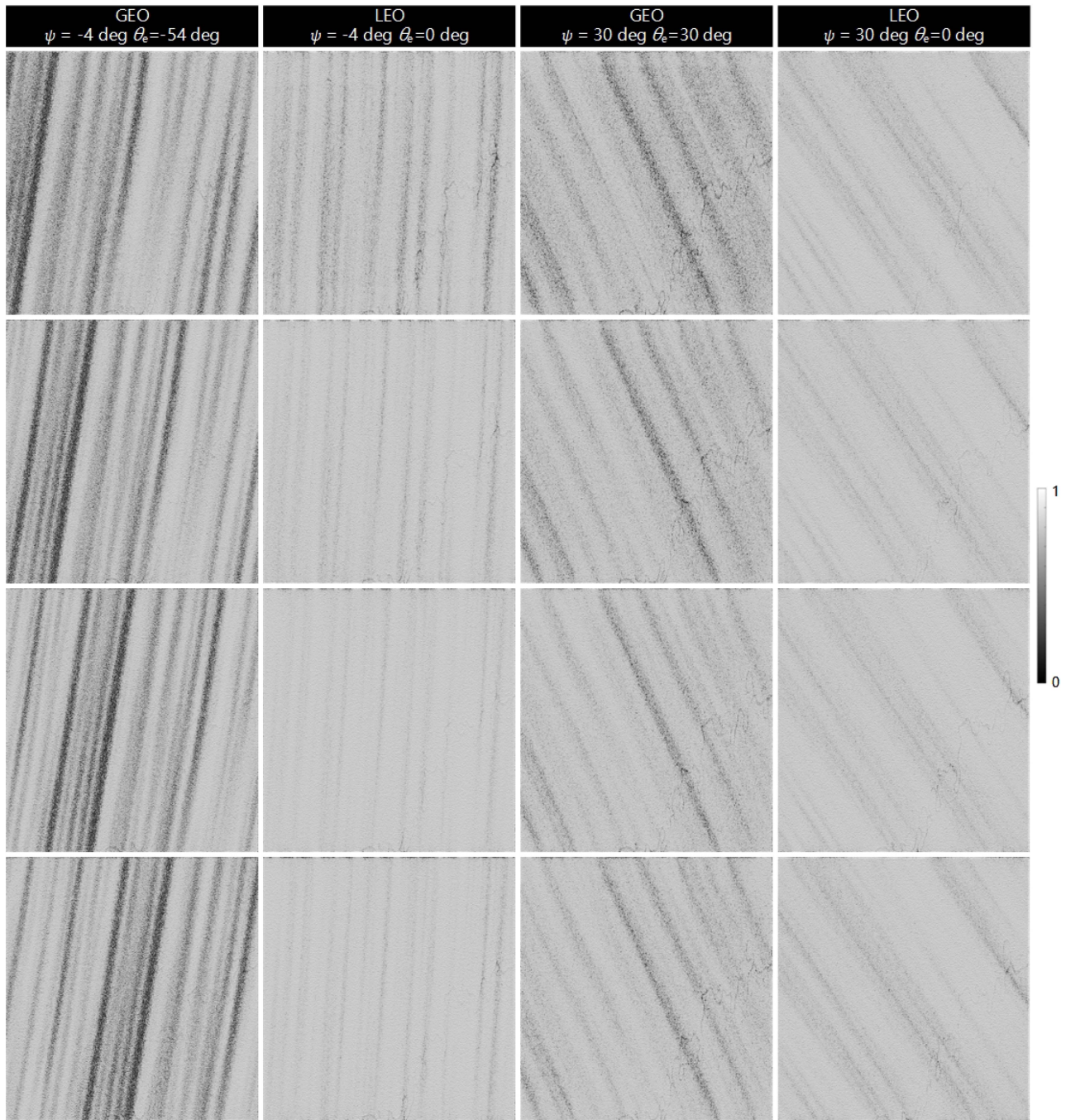


Fig. 10. Sublook complex coherent coefficient by 1/16th sublook-processing. From top row to bottom row, each refers to 2nd, 6th, 10th and 14th subband, respectively.

To sum up, compared with the LEO SAR, the effects of drifting ionospheric irregularities can exactly alter the morphology of the stripe pattern on GEO SAR images. The results of extended-target simulations are in accord with the point-target simulations. The deviation  $|\psi - \theta_e|$  is the crucial factor. For a point target, the amplitude decorrelation within the synthetic aperture is imposed by the scintillation, which can be more serious as  $|\psi - \theta_e|$  increases. At each satellite point, the scintillation phase and amplitude errors are more turbulent as to every single point target. Thus, as to the extended-target, the effects of

drifting irregularities lead to the image defocusing and alter the decorrelation structure with the increasing  $|\psi - \theta_e|$ .

For a further validation, the sublook InSAR coherence are performed to illustrates the effects of drifting ionospheric irregularities according to the pure and contaminated SAR images. Fig. 10 shows the image results of 2nd, 6th, 10th and 14th subband from the top row to bottom row by the 1/16th sublook-processing. The average coherent coefficients are seemingly greater than Fig. 9, because the ionospheric irregularities can have a high coherence in a short period of sublook time. To a certain extent,

the correlation increases compared with the whole band. First, it can be obviously observed that the stripe pattern moves in azimuth of GEO SAR with  $\psi = -4$  deg, which indicates the displacement of the ionospheric irregularities with the effects of drifting. It is consistent with the drifting case of irregularities in Fig. 8. Note that, the displacement of the stripe pattern comes from two components, one refers to the observation geometry of SAR and another refers to the drifting effects of ionospheric irregularities [27]. But the latter can be more significant. Second, as to the LEO SAR with  $\psi = -4$  deg, the stripe pattern is almost stationary. Compare with the GEO SAR, the displacement of ionospheric irregularities in LEO SAR can be much shorter, because the integrated time is much smaller than GEO SAR. Third, the drifting direction of GEO SAR with  $\psi = 30$  deg is almost along the anisotropic extension direction, therefore it is difficult to perceive the displacement of the stripe pattern. Last, as to the LEO SAR with  $\psi = 30$  deg, the displacement of stripe pattern is more subtle.

In a word, the ionospheric PS can have the strongest spatial correlation along the anisotropic extension heading and the weaker spatial correlation across the anisotropic extension heading. Thus, as to the jacent several point targets, when the radio signals propagate through the ionospheric PS along the anisotropic extension heading, the radio signals can be modulated by the highly correlated STFs with the gentle scintillation phase and amplitude errors. As to the point targets distributed across the anisotropic extension heading, the scintillation phase and amplitude errors can be more turbulencing. This is the case that the deviation angle  $|\psi - \theta_e|$  is small enough. Thus, the azimuth imaging performance can improve a lot for a single point-target, and the amplitude stripes eventually come forth on the SAR image, which can be more distinguishable as  $|\psi - \theta_e|$  decreases. The within-aperture decorrelation induced by the ionospheric scintillation leads to the deterioration of the InSAR coherence, and the increasing  $|\psi - \theta_e|$  can lead to the within-aperture decorrelation more serious. In addition, the anisotropic and drifting geometry of the ionospheric irregularities can significantly change the morphology of the amplitude stripes on the GEO SAR images.

## V. CONCLUSION

In this article, we proposed a DISS to generate the L-band GEO SAR raw data affected by the drifting ionospheric scintillation, which can bring about the decorrelation to the SAR signals. The SAR signal model and geometry of trans-ionosphere are proposed based on the ionospheric PS theory, spectrum and drifting mechanism. The DISS can be highly efficient especially in the ultralarge observations, because the procedure takes the relative displacement of the drifting irregularities and static IPP tracking into account. A 2D static PS and STF matrix are sufficient for the echo generation, so that it is no need to generate a 3D PS and STF tensor costing lots of time and memory. The effectiveness is validated by the simulation experiment results, which includes the point-target and extended-target simulations.

The results show that the effects of drifting can exactly influence the azimuth imaging performance, alter the scintillation

morphology and cause more serious decorrelations to the GEO SAR different from the LEO SAR. Next, the InSAR performance is analyzed between the pure and contaminated SAR images. The within-aperture decorrelation can lead to the deterioration of the InSAR coherence and bring about more random perturbations to InSAR phase, and the effects of drifting can lead to the decorrelation more serious. The sublook GEO InSAR coherence can significantly indicate the displacement of the drifting irregularities. As to the GEO SAR, the within-aperture decorrelation is dominated by the deviation angle  $|\psi - \theta_e|$ , which is dependent to both the effects of drifting and anisotropic extension heading. However, the effects of drifting can be reasonably ignored in LEO SAR with  $v_p \gg v_i$  and  $\theta_e \approx 0$ . Thus, the  $|\psi - \theta_e|$  can be regarded as  $|\psi|$ . The anisotropic extension heading  $\psi$  takes over the domination, which is consistent to the existing documents. Last, for the LEO SAR and GEO SAR, the impacts can be different because of the distinct radar altitude.

The works with the DISS are meaningful to the GEO SAR imaging with the effects of drifting irregularities, which has the potential benefits to the future research on ionospheric error compensation and impacts analysis, especially in the lacking of existing GEO SAR real data.

## REFERENCES

- [1] K. Tomiyasu and J. L. Pacelli, "Synthetic aperture radar imaging from an inclined geosynchronous orbit," *IEEE Trans. Geosci. Remote Sens.*, vol. GE-21, no. 3, pp. 324–329, Jul. 1983.
- [2] T. Long et al., *Geosynchronous SAR: System and Signal Processing*. Singapore: Springer, 2018.
- [3] C. Hu et al., "Research progress on geosynchronous synthetic aperture radar," *Fundam. Res.*, vol. 1, pp. 346–363, 2021.
- [4] D. Bruno and S. E. Hobbs, "Radar imaging from geosynchronous orbit: Temporal decorrelation aspects," *IEEE Trans. Geosci. Remote Sens.*, vol. 48, no. 7, pp. 2924–2929, Jul. 2010.
- [5] J. R. Rodon, A. Broquetas, E. Makhoul, A. M. Guarnieri, and F. Rocca, "Nearly zero inclination geosynchronous SAR mission analysis with long integration time for Earth observation," *IEEE Trans. Geosci. Remote Sens.*, vol. 52, no. 10, pp. 6379–6390, Oct. 2014.
- [6] Z. Ding, W. Yin, T. Zeng, and T. Long, "Radar parameter design for geosynchronous SAR in squint mode and elliptical orbit," *IEEE J. Sel. Topics Appl. Earth Observ. Remote Sens.*, vol. 9, no. 6, pp. 2720–2732, Jun. 2016.
- [7] S. Hobbs and J. P. Sanchez, "Laplace plane and low inclination geosynchronous radar mission design," *Sci. China Inf. Sci.*, vol. 60, pp. 1–10, 2017.
- [8] D. Li et al., "Modelling of tropospheric delays in geosynchronous synthetic aperture radar," *Sci. China Inf. Sci.*, vol. 60, pp. 1–18, 2017.
- [9] A. M. Guarnieri, A. Leanza, A. Recchia, S. Tebaldini, and G. Venuti, "Atmospheric phase screen in GEO-SAR: Estimation and compensation," *IEEE Trans. Geosci. Remote Sens.*, vol. 56, no. 3, pp. 1668–1679, Mar. 2018.
- [10] A. Ishimaru et al., "Ionospheric effects on synthetic aperture radar at 100 MHz to 2 GHz," *Radio Sci.*, vol. 34, no. 1, pp. 257–268, 1999.
- [11] Z. Xu, J. Wu, and Z. Wu., "A survey of ionosphere effects on space-based radar," *Waves Random Media.*, vol. 14, no. 2, pp. 189–273, 2004.
- [12] D. P. Belcher, "Theoretical limits on SAR imposed by the ionosphere," *IET Radar, Sonar Navigation*, vol. 2, no. 6, pp. 435–448, 2008.
- [13] F. J. Meyer, "Performance requirements for ionospheric correction of low-frequency SAR data," *IEEE Trans. Geosci. Remote Sens.*, vol. 49, no. 10, pp. 3694–3702, Oct. 2011.
- [14] F. J. Meyer, R. Bamler, N. Jakowski, and T. Fritz, "The potential of low-frequency SAR systems for mapping ionospheric TEC distributions," *IEEE Geosci. Remote Sens. Lett.*, vol. 3, no. 4, pp. 560–564, Oct. 2006.
- [15] F. J. Meyer and J. B. Nicoll, "Prediction, detection, and correction of Faraday rotation in full-polarimetric L-Band SAR data," *IEEE Trans. Geosci. Remote Sens.*, vol. 46, no. 10, pp. 3076–3086, Oct. 2008.

- [16] Y. Zhang, Y. Ji, and Z. Dong, "Distortions imposed by ionospheric Faraday rotation dispersion in low-frequency full-polarimetric SAR images," *IEEE Geosci. Remote Sens. Lett.*, vol. 19, 2022, Art. no. 4003605.
- [17] Y. Tian et al., "Theoretical analysis and verification of time variation of background ionosphere on geosynchronous SAR imaging," *IEEE Geosci. Remote Sens. Lett.*, vol. 12, no. 4, pp. 721–725, Apr. 2015.
- [18] C. Hu, Y. Tian, X. Yang, T. Zeng, T. Long, and X. Dong, "Background ionosphere effects on geosynchronous SAR focusing: Theoretical analysis and verification based on the BeiDou navigation satellite system (BDS)," *IEEE J. Sel. Topics Appl. Earth Observ. Remote Sens.*, vol. 9, no. 3, pp. 1143–1162, Mar. 2016.
- [19] C. Hu et al., "Impacts of temporal-spatial variant background ionosphere on repeat-track GEO D-InSAR system," *Remote Sens.*, vol. 8, 2016, Art. no. 916.
- [20] Y. Ji et al., "Analysis of background ionospheric effects on geosynchronous SAR imaging," *Radioengineering*, vol. 26, no. 1, pp. 130–138, 2017.
- [21] Y. Zhang et al., "Research on background ionospheric irregularities imposed by spatio-temporal variations on spaceborne synthetic aperture radar azimuth imaging," *J. Electron. Inf. Technol. (in Chinese)*, vol. 43, no. 10, pp. 2781–2789, 2021.
- [22] C. Wang, M. Zhang, Z.-W. Xu, C. Chen, and D.-S. Sheng, "Effects of anisotropic ionospheric irregularities on space-borne SAR imaging," *IEEE Trans. Antennas Propag.*, vol. 62, no. 9, pp. 4664–4673, Sep. 2014.
- [23] Y. Ji, Q. Zhang, Y. Zhang, Z. Dong, and B. Yao, "Spaceborne P-band SAR imaging degradation by anisotropic ionospheric irregularities: A comprehensive numerical study," *IEEE Trans. Geosci. Remote Sens.*, vol. 58, no. 8, pp. 5516–5526, Aug. 2020.
- [24] F. J. Meyer, K. Chotoo, S. D. Chotoo, B. D. Huxtable, and C. S. Carrano, "The influence of equatorial scintillation on L-band SAR image quality and phase," *IEEE Trans. Geosci. Remote Sens.*, vol. 54, no. 2, pp. 869–880, Feb. 2016.
- [25] D. P. Belcher and P. S. Cannon, "Amplitude scintillation effects on SAR," *IET Radar Sonar Navigation*, vol. 8, no. 6, pp. 658–666, 2014.
- [26] C. S. Carrano, M. K. Groves, and G. R. Caton, "Simulating the impacts of ionospheric scintillation on L-band SAR image formation," *Radio Sci.*, vol. 70, no. RS0L20, pp. 1–14, 2012.
- [27] J. S. Kim, K. Papathanassiou, H. Sato, and S. Quegan, "Detection and estimation of equatorial spread F scintillations using synthetic aperture radar," *IEEE Trans. Geosci. Remote Sens.*, vol. 55, no. 12, pp. 6713–6725, Dec. 2017.
- [28] N. Gan, Y. Ji, F. Tang, Y. Zhang, and Z. Dong, "Correcting and measuring ionospheric scintillation amplitude stripes in L-band SAR images," *IEEE Geosci. Remote Sens. Lett.*, vol. 19, 2022, Art. no. 4515505.
- [29] Y. Ji, Y. Zhang, Q. Zhang, and Z. Dong, "Comments on The influence of equatorial scintillation on L-band SAR image quality and phase," *IEEE Trans. Geosci. Remote Sens.*, vol. 57, no. 9, pp. 7300–7301, Sep. 2019.
- [30] J. S. Kim, K. P. Papathanassiou, R. Scheiber, and S. Quegan, "Correcting distortion of polarimetric SAR data induced by ionospheric scintillation," *IEEE Trans. Geosci. Remote Sens.*, vol. 53, no. 12, pp. 6319–6335, Dec. 2015.
- [31] Y. Ji et al., "Extended scintillation phase gradient autofocus in future spaceborne P-band SAR mission," *Sci. China Inf. Sci.*, vol. 64, 2021, Art. no. 212303.
- [32] Y. Ji, C. Yu, Q. Zhang, Z. Dong, Y. Zhang, and Y. Wang, "An ionospheric phase screen projection method of phase gradient autofocus in spaceborne SAR," *IEEE Geosci. Remote Sens. Lett.*, vol. 19, 2022, Art. no. 4504205.
- [33] C. Gracheva, J. S. Kim, P. Prats-Iraola, R. Scheiber, and M. Rodriguez-Cassola, "Combined estimation of ionospheric effects in SAR images exploiting Faraday rotation and autofocus," *IEEE Geosci. Remote Sens. Lett.*, vol. 19, 2022, Art. no. 8018705.
- [34] D. P. Belcher, C. R. Mannix, and P. S. Cannon, "Measurement of the ionospheric scintillation parameter CkL from SAR images of clutter," *IEEE Trans. Geosci. Remote Sens.*, vol. 55, no. 10, pp. 5937–5943, Oct. 2017.
- [35] C. R. Mannix, D. P. Belcher, and P. S. Cannon, "Measurement of ionospheric scintillation parameters from SAR images using corner reflectors," *IEEE Trans. Geosci. Remote Sens.*, vol. 55, no. 12, pp. 6695–6702, Dec. 2017.
- [36] Y. Ji, Z. Dong, Y. Zhang, and Q. Zhang, "An autofocus approach with applications to ionospheric scintillation compensation for spaceborne SAR images," *IEEE Trans. Aerosp. Electron. Syst.*, vol. 58, no. 2, pp. 989–1004, Apr. 2022.
- [37] Y. Ji, Z. Dong, Y. Zhang, Q. Zhang, L. Yu, and B. Qin, "Measuring ionospheric scintillation parameters from SAR images using phase gradient autofocus: A case study," *IEEE Geosci. Remote Sens.*, vol. 60, 2022, Art. no. 5200212.
- [38] Y. Li et al., "Impacts of ionospheric scintillation on geosynchronous SAR focusing: Preliminary experiments and analysis," *China Sci. Inform. Sci.*, vol. 58, 2015, Art. no. 109301.
- [39] X. Dong, C. Hu, Y. Tian, W. Tian, Y. Li, and T. Long, "Experimental study of ionospheric impacts on geosynchronous SAR using GPS signals," *IEEE J. Sel. Topics Appl. Earth Observ. Remote Sens.*, vol. 9, no. 6, pp. 2171–2183, Jun. 2016.
- [40] C. Hu, Y. Li, X. Dong, R. Wang, and D. Ao, "Performance analysis of L-band Geosynchronous SAR imaging in the presence of ionospheric scintillation," *IEEE Trans. Geosci. Remote Sens.*, vol. 55, no. 1, pp. 159–172, Jan. 2017.
- [41] R. Wang et al., "Joint amplitude-phase compensation for ionospheric scintillation in GEO SAR imaging," *IEEE Trans. Geosci. Remote Sens.*, vol. 55, no. 6, pp. 3454–3465, Jun. 2017.
- [42] Y. Ji et al., "L-band geosynchronous SAR imaging degradations imposed by ionospheric irregularities," *China Inform. Sci.*, vol. 60, 2017, Art. no. 060308.
- [43] Y. Ji, Y. Zhang, Z. Dong, Q. Zhang, D. Li, and B. Yao, "Impacts of ionospheric irregularities on L-band geosynchronous synthetic aperture radar," *IEEE Trans. Geosci. Remote Sens.*, vol. 58, no. 6, pp. 3941–3954, Jun. 2020.
- [44] Y. Ji, Z. Dong, and Y. Zhang, "Geosynchronous SAR raw data simulator in presence of ionospheric scintillation using reverse backprojection," *Electron. Lett.*, vol. 56, no. 10, pp. 512–514, 2020.
- [45] C. Rino, "A power law phase screen model for ionospheric scintillation I. Weak scatter," *Radio Sci.*, vol. 14, no. 6, pp. 1135–1145, 1979.
- [46] C. L. Rino, *The Theory of Scintillation With Applications in Remote Sensing*. New York, NY, USA: Wiley, 2011.
- [47] F. Tang et al., "Ionospheric phase scintillation correction based on multi-aperture Faraday rotation estimation in spaceborne P-band full-polarimetric SAR data," *Remote Sens.*, vol. 14, 2022, Art. no. 5659.
- [48] I. P. Shkarofsky, "Turbulence functions useful for probes and for scattering analysis," *Can. J. Phys.*, vol. 46, pp. 2683–2702, 1968.
- [49] K. C. Yeh and C.-H. Liu, "Radio wave scintillations in the ionosphere," *Proc. IEEE*, vol. 70, no. 4, pp. 324–360, Apr. 1982.
- [50] B. G. Fejer, "Low latitude electrodynamic plasma drifts - A review," *J. Atmos. Sol. Terr. Phys.*, vol. 53, no. 8, pp. 677–693, 1991.
- [51] X. Ma and H. Fang, "Optical observation of plasma bubbles and comparative study of multiple methods of observing the ionosphere over China," *Adv. Space Res.*, vol. 65, no. 12, pp. 2761–2772, 2020.
- [52] N. C. Rogers, C. S. Carrano, and M. K. Groves, "Measurements and simulation of ionospheric scattering on VHF and UHF radar signals: Channel scattering function," *Radio Sci.*, vol. 40, no. RS0A07, pp. 1–10, 2009.



**Feixiang Tang** was born in Yongzhou of Hunan Province, China, in 1999. He received the B.S. degree in electronic information science from Harbin Engineering University, Harbin, China, College of Information and Communication Engineering, in 2021. He is currently working toward the Ph.D. degree in information and communication engineering from National University of Defense Technology, College of Electronic Science and Technology, Changsha, China.

His research interests include radar imaging, synthetic aperture radar, ionospheric electromagnetic wave propagation and ionospheric impacts.

**Yifei Ji** (Member, IEEE) was born in Jiangyin of Jiangsu Province, China, in 1992. He received the B.S. degree in electronic information engineering from the Nanjing University of Science and Technology, Nanjing, China, in 2014, and the M.S. degree in information and communication engineering from the National University of Defense Technology (NUDT), Changsha, China, in 2016. He is currently working toward the Ph.D. degree with the College of Electronic Science, NUDT.

His research interests include radar signal processing, synthetic aperture radar, and ionospheric impacts.

**Yongsheng Zhang** was born in Inner Mongolia, China, in December 1977. He received the Ph.D. degree in electronics and information engineering from the National University of Defense Technology, Changsha, China, in 2007.

He is currently a Professor with the College of Electronic Science and Technology, National University of Defense Technology. His current research interests include SAR system design and SAR data processing.

**Zhen Dong** was born in Anhui, China, in September 1973. He received the Ph.D. degree in electrical engineering from the National University of Defense Technology (NUDT), Changsha, China, in 2001.

He is currently a Professor with the College of Electronic Science and Engineering, NUDT. His recent research interests include SAR system design and processing, ground moving target indication (GMTI), and digital beamforming (DBF).

**Zhaokai Wang** received the B.S. degree in electronic information science from Harbin Engineering University, College of Information and Communication Engineering, Harbin, China, in 2021. He is currently working toward the M.S. degree in information and communication engineering from National University of Defense Technology (NUDT), College of Electronic Science and Technology, Changsha, China.

His research interests include ionospheric electromagnetic wave propagation and radiowave propagation.

**Qingjun Zhang** was born in Xuzhou, Jiangsu, China, in 1969. He received the Ph.D. degree in information and communication engineering from the Huazhong University of Science and Technology, Wuhan, China, in 2004.

He is currently a Professor of Satellite Engineering with the China Academy of Space Technology (CAST), Beijing, China. He is also the Program Manager and the Chief Engineer of GF-3 and HY-2 programs, and the Chief Engineer of China, Brazil Earth Remote Sensing Satellite. He is also involved in the research of microwave remote sensing, especially in the synthetic aperture radar.

Dr. Zhang is a member of Technical Committee with CAST.

**Bingji Zhao** received the B.S. degree in electronic engineering and information science from the Ha'er Bin Engineering University, Heilongjiang, China, in 2007, and the Ph.D. degree in communication and information system from the Institute of Electronics, University of Chinese Academy of Science, Beijing, China, in 2013.

In 2013, he joined the Beijing Institute of Spacecraft System Engineering in CAST, where he was currently funded by Outstanding Young Scientists in CAST. He is currently a Senior Engineer and has been the Technical Director of several spaceborne SAR satellite and one airborne SAR programs. His current research interests include geosynchronous synthetic aperture radar (Geo-SAR) and Low Earth orbital high-resolution Spaceborne SAR system designing and 3-D SAR imaging techniques.

**Heli Gao** received the Ph.D. degree in signal and information processing from BeiHang University, Beijing, China, in 2020.

He is currently working with the Institute of Remote Sensing Satellite China Academy of Space Technology Beijing, China. His current research interests include ionospheric electromagnetic wave propagation, radar imaging, radiowave propagation, remote sensing, synthetic aperture radar.